



HAL
open science

The CH₄ abundance in Jupiter's upper atmosphere

A. Sánchez-López, M. López-Puertas, M. García-Comas, B. Funke, T. Fouchet, I. A. G. Snellen

► **To cite this version:**

A. Sánchez-López, M. López-Puertas, M. García-Comas, B. Funke, T. Fouchet, et al.. The CH₄ abundance in Jupiter's upper atmosphere. *Astronomy and Astrophysics - A&A*, 2022, 662, 10.1051/0004-6361/202141933 . insu-03713301

HAL Id: insu-03713301

<https://insu.hal.science/insu-03713301>

Submitted on 4 Jul 2022

HAL is a multi-disciplinary open access archive for the deposit and dissemination of scientific research documents, whether they are published or not. The documents may come from teaching and research institutions in France or abroad, or from public or private research centers.

L'archive ouverte pluridisciplinaire **HAL**, est destinée au dépôt et à la diffusion de documents scientifiques de niveau recherche, publiés ou non, émanant des établissements d'enseignement et de recherche français ou étrangers, des laboratoires publics ou privés.

The CH₄ abundance in Jupiter's upper atmosphere

A. Sánchez-López¹ , M. López-Puertas² , M. García-Comas² , B. Funke², T. Fouchet³, and I. A. G. Snellen¹

¹ Leiden Observatory, Leiden University, Postbus 9513, 2300 RA Leiden, The Netherlands
e-mail: alexsl@strw.leidenuniv.nl

² Instituto de Astrofísica de Andalucía (IAA-CSIC), Glorieta de la Astronomía s/n, 18008 Granada, Spain

³ LESIA, Observatoire de Paris, Université PSL, CNRS, Sorbonne Université, Université de Paris, 5 place Jules Janssen, 92195 Meudon, France

Received 2 August 2021 / Accepted 19 February 2022

ABSTRACT

Hydrocarbon species, and in particular CH₄, play a key role in the stratosphere–thermosphere boundary of Jupiter, which occurs around the μ -bar pressure level. Previous analyses of solar occultation, He and Ly- α airglow, and ISO/SWS measurements of the radiance around 3.3 μ m have inferred significantly different methane concentrations. Here we aim to accurately model the CH₄ radiance at 3.3 μ m measured by ISO/SWS by using a comprehensive non-local thermodynamic equilibrium model and the most recent collisional rates measured in the laboratory for CH₄ to shed new light onto the methane concentration in the upper atmosphere of Jupiter. These emission bands have been shown to present a peak contribution precisely at the μ -bar level, hence directly probing the region of interest. We find that a high CH₄ concentration is necessary to explain the data, in contrast with the most recent analyses, and that the observations favour the lower limit of the latest laboratory measurements of the CH₄ collisional relaxation rates. Our results provide precise constraints on the composition and dynamics of the lower atmosphere of Jupiter.

Key words. planets and satellites: atmospheres – methods: data analysis - techniques: spectroscopic – planets and satellites: individual: Jupiter

1. Introduction

The energy budget in the stratosphere–thermosphere boundary of the atmosphere of Jupiter ($\sim 10^{-3}$ mbar) is largely governed by radiative processes (Appleby 1990; Moses et al. 2005; Miller et al. 2013). In these layers methane (CH₄) is the most abundant spectroscopically active hydrocarbon species absorbing solar radiation. The incoming flux induces rotations and vibrations in the two bending and two stretching modes of CH₄ (see e.g. García-Comas et al. 2011), giving rise to strong emissions in the CH₄ near-IR bands that can be observed in the daylight atmosphere of Jupiter.

At the μ -bar level the methane abundance is determined by photolysis, which initiates a rich hydrocarbon chemistry (see Fig. 9 in Moses et al. 2005). At lower pressures (higher altitudes), the competition between eddy and molecular diffusion results in a decrease in hydrocarbon coolants (including CH₄) in the lower thermosphere, giving rise to the observed temperature inversion (Yelle et al. 1996; Moses et al. 2005). In this context, accurately constraining the abundance of methane at the homopause is key to understanding the complex dynamics, the thermal structure, and the composition of the upper atmosphere of Jupiter. Unfortunately, the CH₄ concentration has not been measured in situ, but it is commonly inferred from its nadir radiance at 3.3 μ m in the daylight, which has been shown to probe the 10^{-1} – 10^{-4} mbar pressure layers (Kim et al. 2009, 2014, 2020). Previous studies along this line analysed the Infrared Space Observatory (ISO, Kessler et al. 1996; de Graauw 1996) measurements of CH₄ emission in the atmosphere of Jupiter using its Short Wavelength Spectrometer (SWS, Encrenaz et al. 1999; Drossart et al. 1999; Kim et al. 2014, 2020; Panka et al. 2018).

In particular, Drossart et al. (1999) were able to nicely reproduce the ISO nadir spectrum by adjusting two collisional parameters in their non-local thermodynamic equilibrium (non-LTE) model and an eddy diffusion coefficient (k_{zz}) at the homopause in the range of $(6\text{--}8) \times 10^6$ cm² s⁻¹. These k_{zz} are similar to those of model A in Moses et al. (2005), and hence point to a rather high CH₄ volume mixing ratio (VMR) (see e.g. Fig. 14a in Moses et al. 2005). Drossart et al. (1999) did not discuss the sensitivity to different pressure-temperature (p-T) profiles, and they also assumed collisional rates for the thermalisation of the solar pumped vibrational states by collisions with H₂ and for the intergroup redistribution of the absorbed energy which are about 20 and 10 times smaller, respectively, than those measured for the lower-energy states by Menard-Bourcin et al. (2005) a few years later.

Subsequently, Kim et al. (2014) analysed the ISO/SWS Jupiter spectra finding CH₄ VMRs significantly lower than those derived by Drossart et al. (1999) and Moses et al. (2005), with an upper limit of $\sim 6 \times 10^{-5}$ at 10^{-3} mbar. Although they did not report the populations of the emitting states, it is likely that this finding was caused by the rather low collisional rates they used (in comparison to those measured by Menard-Bourcin et al. 2005), which resulted in a slow thermalisation for the highly excited solar-pumped emitting states.

Interestingly, the nominal calculations of Kim et al. (2014) (models A and D) significantly underestimate the ISO radiance originating from the hot band ($v_3+v_4 \rightarrow v_4$) centred near 3.325 μ m. They did not focus specifically on this band, although its emission contains significant information that could help us constrain the collisional rates of high-energy states in order to better estimate the possible excitation of the v_3 state from the deactivation

of the v_3+v_4 level, and possibly to retrieve the CH_4 concentration at pressure levels of $\sim 10^{-2}$ mbar.

More recently, Kim et al. (2020) revised their analysis using the collisional rates from Menard-Bourcin et al. (2005). The authors obtained significantly higher CH_4 abundances at the μ -bar level than in their previous study, but still lower than those of Drossart et al. (1999). However, we argue in Sect. 6.1 that this might be due to a misuse of the laboratory measurements of Menard-Bourcin et al. (2005).

Here we re-examine the ISO/SWS observations of the CH_4 fluorescence near $3.3 \mu\text{m}$ using a comprehensive non-LTE model for this molecule, also including the most recent measurements of the collisional rates by Menard-Bourcin et al. (2005) so as to fully exploit the information content of this spectrum. In particular, we our aim is to distinguish between the divergent CH_4 VMR profiles derived so far from the nadir ISO measurements. We describe the ISO/SWS measurements and their calibration in Sect. 2. In Sects. 3 and 4 respectively we describe the non-LTE model and the model Jupiter atmospheres we used to obtain the results presented in Sect. 5 and discussed in Sect. 6. Finally, in Sect. 7 we summarise the main conclusions of this work.

2. Observations

The nadir observations of the atmosphere of Jupiter were obtained on May 25, 1997 (UT), using the ISO/SWS spectrometer, which covers the $2.38\text{--}45.2 \mu\text{m}$ spectral region (de Graauw 1996). We restricted the analysis to the $3.20\text{--}3.45 \mu\text{m}$ interval (band 1D, grating order SW3), where CH_4 emits, using its grating mode with a resolving power of $1750\text{--}2150$ (Encrenaz et al. 1999). The observations were taken by pointing the instrumental $14 \times 20 \text{ arcsec}^2$ aperture at Jupiter's centre (Drossart et al. 1999; Encrenaz et al. 1999), while the solar zenith angle in the planet atmosphere was nearly 0 deg . The aperture was aligned with its long-axis, roughly parallel to the planet's polar axis. It covered latitudes in the range $\pm 30^\circ$ and longitudes in the range $\pm 20^\circ$ from the central meridian. The measured infrared spectrum is shown in Fig. 8 and details about the reduction, calibration, and uncertainties are provided in de Graauw (1996) and Encrenaz et al. (1999). In particular, Encrenaz et al. (1999) reported a 3σ value of ± 1 jansky. In the following, we use the corresponding 1σ uncertainties in units of $\text{W}/(\text{m}^2 \text{ sr } \mu\text{m})$. The absolute flux accuracy is of the order of 20% . In addition, we found that the best fit was obtained when applying a spectral offset of $-3 \times 10^{-5} \mu\text{m}$.

3. The CH_4 non-LTE model

The CH_4 non-LTE model used here is essentially that described in detail by García-Comas et al. (2011); it is based on the Generic RAdiative traNsfEr AnD non-LTE population Algorithm (GRANADA), originally built specifically for the Earth's atmosphere (Funke et al. 2012). This non-LTE model was successfully applied to explain the methane $3.3 \mu\text{m}$ atmospheric emission observed by the Visible and Infrared Mapping Spectrometer instrument on board the Cassini spacecraft in the atmosphere of Titan. The bulk composition of Titan's atmosphere is of N_2 , whereas the atmosphere of Jupiter contains mainly H_2 and He, and hence we adapted our model to reflect the physical conditions of this gas giant and the different collisional partners and rates of the CH_4 vibrational states.

The energy levels and radiative transitions considered are illustrated in Fig. 1 (see also Fig. 2 in García-Comas et al. 2011) and listed in Tables B.1 and B.2. We considered four groups of

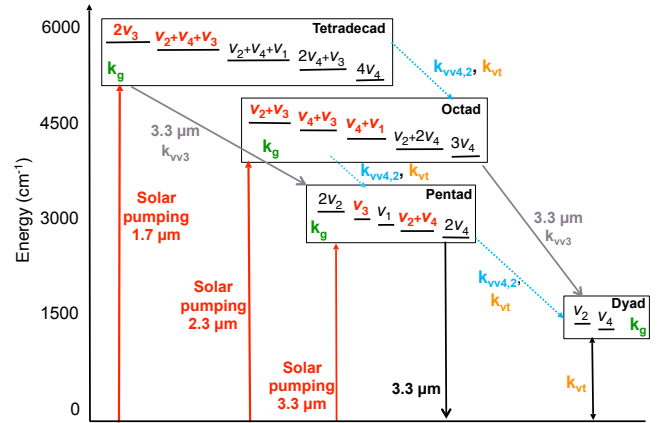


Fig. 1. Energy levels and groups, radiative transitions, and collisional processes considered in this work for the main isotope of CH_4 . The solar-pumped energy levels are indicated in red. Adapted from García-Comas et al. (2011).

energy levels (polyads) that involve the four fundamental modes of vibration of the main isotope of CH_4 . Namely, the bending modes v_2 (symmetric) and v_4 (asymmetric), and the stretching modes v_1 (symmetric) and v_3 (asymmetric). The grouping facilitated the computation of collisional processes involving many levels, but individual populations were computed separately for each of them. That is, we did not assume the levels in a given group to be in LTE among themselves. In addition to the main $^{12}\text{CH}_4$ isotopologue levels, we also included the v_4 , $2v_4$, and v_3 states of the second most abundant $^{13}\text{CH}_4$ isotopologue. The energy levels listed above are coupled by the collisional processes listed in Table 1 (discussed below) and, in addition, they are considered to be inter-connected by the vibrational bands listed in Table B.2. As some of these bands are rather weak, it was not necessary to take into account the exchange of photons between atmospheric layers due to radiative excitation or deexcitation. The bands for which radiative transfer was included are flagged ‘RT’ in Table B.2.

The resulting system of equations is then composed of the statistical equilibrium equation for the energy levels involved and the radiative transfer equations for the corresponding vibrational bands. It was solved by a combination of the Curtis matrix and lambda iteration methods. For more details, see Sect. 9 in Funke et al. (2012). The spectroscopic data used for the calculation of the non-LTE populations described in this section and for the nadir radiance (see Sect. 4.2) were mainly taken from the HITRAN 2016 compilation (Gordon et al. 2017). Some CH_4 bands in that compilation are incomplete as some predicted ro-vibrational lines included in previous HITRAN editions were removed. We replaced these bands by the corresponding ones of the HITRAN 2012 compilation (Rothman et al. 2013). In addition, some of the high-energy levels are connected through vibrational bands that are missing in those compilations and were taken from the MeCaSDa database (Ba et al. 2013). Table B.2 lists all the bands with their Einstein coefficients and respective sources.

The excitation of the CH_4 levels in the stratosphere and thermosphere of Jupiter is triggered by solar pumping in the near-infrared. Table B.2 indicates the bands where absorption of solar radiation was included. The spectral solar flux at 1 AU included in this work for this spectral region was described in detail in Jurado-Navarro et al. (2015) and was adapted to the Sun–Jupiter distance at the time of the observations.

Table 1. Collisional processes included in the CH₄ non-LTE model.

No.	Process	Col. partner	Rate [†] (cm ³ s ⁻¹)	Reference
1a	CH ₄ (<i>v</i> ₁ , <i>v</i> ₃ , <i>v</i> _{<i>b</i>})+M⇌	M=H ₂ , He	$k_{g,a} = 2.45 \times 10^{-11} (0.237 + 2.58 \times 10^{-3} T)$	1
	CH ₄ (<i>v</i> ₁ +1, <i>v</i> ₃ -1, <i>v</i> _{<i>b</i>})+M	M=CH ₄	$k_{g,a,CH_4} = 1.0 \times 10^{-11} (1.157 + 7.48 \times 10^{-3} T)$	1
1b	CH ₄ (<i>v</i> _{<i>s</i>} , <i>v</i> ₂ , <i>v</i> ₄)+M⇌	M=H ₂ , He	$k_{g,b} = 3.68 \times 10^{-11} (0.313 + 2.32 \times 10^{-3} T)$	1
	CH ₄ (<i>v</i> _{<i>s</i>} , <i>v</i> ₂ -1, <i>v</i> ₄ +1)+M	M=CH ₄	$k_{g,b,CH_4} = 1.0 \times 10^{-11} (1.146 + 18.9 \times 10^{-3} T)$	1
1c	CH ₄ (<i>v</i> ₃ , <i>v</i> _{<i>b</i>})+M⇌	M=H ₂ , He	$k_{g,c} = 3.53 \times 10^{-11} (-0.57 + 5.31 \times 10^{-3} T)$	1
	CH ₄ (<i>v</i> ₃ -1, <i>v</i> _{<i>b</i>} + <i>v</i> ₂ + <i>v</i> ₄)+M	M=CH ₄	$k_{g,c,CH_4} = 1.0 \times 10^{-11} (1.726 + 9.71 \times 10^{-3} T)$	1
1d ^(*)	CH ₄ (<i>v</i> ₃ , <i>v</i> _{<i>b</i>})+M⇌	M=H ₂ , He, CH ₄	$k_{g,d} = 1.0 \times 10^{-12} (0.976 + 5.49 \times 10^{-3} T)$	2
	CH ₄ (<i>v</i> ₃ -1, <i>v</i> _{<i>b</i>} +2 <i>v</i> ₄)+M			
2	CH ₄ ^{<i>i</i>} (<i>v</i> ₁ , <i>v</i> ₃ , <i>v</i> _{<i>b</i>})+M⇌	M=H ₂	$k_{vt,H_2} = v_b \cdot 2.48 \times 10^{-14} \exp(9.11 \times 10^{-3} T)$	1
	CH ₄ ^{<i>i</i>} (<i>v</i> ₁ , <i>v</i> ₃ , <i>v</i> _{<i>b</i>} -1)+M	M=He	$k_{vt,He} = v_b \cdot 6.37 \times 10^{-16} \exp(0.01111 T)$	1
		M=CH ₄	$k_{vt,CH_4} = v_b \cdot 10^{-16} \exp(0.0347 T - 5.14 \times 10^{-5} T^2)$	1
3a	CH ₄ (<i>v</i> _{<i>s</i>} , <i>v</i> ₄)+CH ₄ ⇌CH ₄ (<i>v</i> _{<i>s</i>} , <i>v</i> ₄ -1)+CH ₄ (<i>v</i> ₄)		$k_{vv,4} = v_4 \cdot 1.1 \times 10^{-11}$	1
3b	CH ₄ (<i>v</i> _{<i>s</i>} , <i>v</i> ₂)+CH ₄ ⇌CH ₄ (<i>v</i> _{<i>s</i>} , <i>v</i> ₂ -1)+CH ₄ (<i>v</i> ₂)		$k_{vv,2} = v_2 \cdot 1.1 \times 10^{-11}$	3
3c	CH ₄ (<i>v</i> ₃ , <i>v</i> _{<i>b</i>})+CH ₄ ⇌CH ₄ (<i>v</i> ₃ -1, <i>v</i> _{<i>b</i>})+CH ₄ (<i>v</i> ₃)		$k_{vv,3} = v_3 \cdot 2.6 \times 10^{-12}$	1
4a	CH ₄ ^{<i>i</i>} (<i>v</i> _{<i>s</i>} , <i>v</i> _{<i>b</i>})+CH ₄ ^{<i>j</i>} ⇌CH ₄ ^{<i>i</i>} (<i>v</i> _{<i>s</i>} , <i>v</i> _{<i>b</i>} -1)+CH ₄ ^{<i>j</i>} (<i>v</i> _{<i>b</i>} =1)		$k_{vv4,iso} = 1.1 \times 10^{-11}$	3
4b	CH ₄ ^{<i>i</i>} (<i>v</i> _{<i>s</i>} , <i>v</i> _{<i>b</i>})+CH ₄ ^{<i>j</i>} ⇌CH ₄ ^{<i>i</i>} (<i>v</i> _{<i>s</i>} -1, <i>v</i> _{<i>b</i>})+CH ₄ ^{<i>j</i>} (<i>v</i> _{<i>s</i>} =1)		$k_{vv3,iso} = 2.6 \times 10^{-12}$	3

Notes. [†]Rate coefficient for the forward direction of the process. Backward values are computed assuming detailed balance (see e.g. Eq. (3.54) of López-Puertas & Taylor 2001). *v_b* is the bending quantum (*v*₂ or *v*₄). *v_s* is the stretching quantum (*v*₁ or *v*₃). ^(*)Not considered in the nominal model. *i* and *j* refer to isotopologues ¹²CH₄ and ¹³CH₄, respectively. Rates at temperatures below 160 K and above 350 K are fixed to the values at those temperatures, respectively.

References. (1) Menard-Bourcin et al. (2005); (2) Hess & Moore (1976); (3) this work.

The collisional scheme implemented in this work (the nominal model) follows the laboratory measurements and subsequent analysis of Menard-Bourcin et al. (2005), who studied collisions between the excited states of CH₄ with H₂, He, and other CH₄ molecules. They considered three main types of energy transfer processes: (i) intermode energy transfer; (ii) V–T (vibrational-thermal) energy transfer, and (iii) near-resonant vibration-vibration energy transfer processes. The intermode energy transfer processes redistribute the absorbed solar energy among the levels within a polyad through collisions with H₂, He, and CH₄. These processes comprise the energy transfer among the (i) stretching modes (*v*₃⇌*v*₁); (ii) bending modes (*v*₂⇌*v*₄); and (iii) stretching and bending modes (2*v*_{*b*}⇌*v*_{*s*}; see processes 1a, 1b, and 1c, respectively, in Table 1). The processes in (iii) can be of different types depending on the initial stretching mode, *v*₁ or *v*₃, and the final bending mode, 2*v*₄ or *v*₂+*v*₄. Here we follow Menard-Bourcin et al. (2005) and, in our nominal model, we consider only the *v*₃→*v*₂+*v*₄ path (process 1c). Other authors (e.g. Hess et al. 1980; Kim et al. 2014) have considered that the main relaxation of the *v*₃ state occurs through *v*₃→2*v*₄ (process 1d). As the resulting populations of the CH₄ excited states strongly depend on the assumed relaxation path, we studied both possibilities (see Sect. 6).

The V-T energy transfer processes are responsible for the final relaxation of vibrational energy (pumped by absorption of solar radiation) into thermal energy. These processes are usually much slower than the intermode and V-V self-energy redistribution and involve the transitions where the transferred energy is the lowest possible (e.g. through the *v*₄ and *v*₂ bending quanta; see process 2 in Table 1). We note that these processes couple the energy levels among different polyads (Fig. 1).

The near-resonant vibration-vibration energy transfer processes are assumed to occur only upon CH₄ self-collisions.

These processes redistribute the energy among polyads by exchanging one *v*₄ or one *v*₂ quanta, and by exchanging one *v*₃ quantum (see processes 3a, 3b, and 3c in Table 1). Similar vibration-vibration energy transfer processes between the two considered isotopologues of CH₄ are also included (processes 4a and 4b in Table 1).

The values of the rates of the collisional processes are from Menard-Bourcin et al. (2005) and were measured at 193 and 296 K. We fitted the expressions in Table 1 to the measured values. At temperatures below 160 K and above 350 K we considered the values at 160 and 350 K, respectively. In the derivation of the measured rates, Menard-Bourcin et al. (2005) assumed that all *v*₃→*v*₁ intermode transfer processes (i.e. irrespective of the *v*_{*b*} excitation of the states) have the same rate coefficients for a given collisional partner. Regarding the near resonant V–V processes, they are scaled by the factor predicted with the first-order perturbation theory for harmonic oscillators. The same approach was used for the rate coefficients of the V–T transfer processes (process 2 in Table 1). In addition to the V–V transfer of *v*₄ in Menard-Bourcin et al. (2005), we included a similar process with the exchange of a *v*₂ quanta for which we assumed the same value. Near-resonant V–V transfer processes for *v*₄ and *v*₃ exchanges between CH₄ isotopologues were also included in our scheme. For these we assumed the same rate coefficients measured by Menard-Bourcin et al. (2005) for similar processes in the main isotopologue. Processes 1–3 in Table 1 were also considered assuming the rate coefficients for both isotopologues.

Figure 2 shows the resulting daytime (SZA = 0°) vibrational temperatures of the energy levels of CH₄ with energies close to and larger than 3.3 μm for the nominal profile p-T₁, the CH₄ volume mixing ratio VMR₁ (see Sect. 4), and the nominal collisional rates of the non-LTE model (Table 1). We observed that the *v*₃ level, the major contributor to the 3.3 μm radiance,

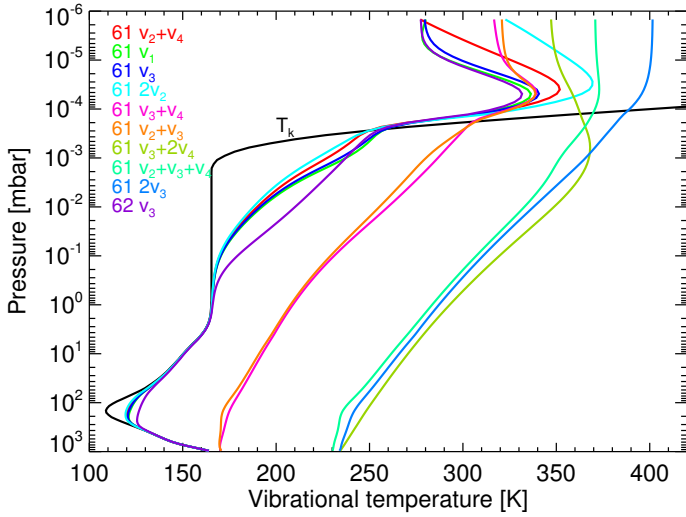


Fig. 2. Daytime ($SZA = 0^\circ$) vibrational temperatures of the main CH_4 energy levels contributing to the $3.3 \mu m$ radiance as a function of pressure. The $p-T_1$ kinetic temperature profile, the VMR_1 abundance profile, and the nominal collisional rates of Table 1 were used. The major CH_4 isotopologue is labelled ‘61’ and the second is labelled ‘62’.

remains in LTE at pressures higher than $\sim 10^{-1}$ mbar, whereas the v_3+v_4 level is significantly far from LTE conditions in this region. At higher altitudes, v_3 departs from LTE and thus decouples from the kinetic temperature (T_k). Although both levels remain in non-LTE at lower pressures, the strong kinetic temperature inversion of $p-T_1$ at pressures below 10^{-3} mbar impacts their vibrational temperatures, which peak at $\sim 5 \times 10^{-5}$ mbar. At higher altitudes and at pressures lower than $\sim 10^{-6}$ mbar the T_{vib} of both levels become isothermal since they are almost completely decoupled from T_k due to the very low atmospheric density. The vibrational temperatures of the more energetic energy levels are significantly higher and more decoupled from LTE. This is mainly due to the high-frequency solar flux penetrating deeper in the atmosphere and due to the less efficient deexcitations for these high-energy levels. We note that the vibrational temperatures of these energy levels near 10^{-3} mbar depend very closely on the collisional rates (see Sect. 5.2).

4. Atmospheric modelling

4.1. Inputs for the CH_4 abundance and pressure-temperature structures

The measured radiance in a nadir sounding depends firstly and most importantly on the density of the emitting gas, CH_4 in our case, which dictates the atmospheric region where the emission emanates. Secondly, it depends on the population of the emitting levels. The latter are controlled by the kinetic temperature under LTE conditions, and by the vibrational temperatures under non-LTE, which might also depend, although more weakly, on the kinetic temperature profile itself.

We explored several abundance profiles of CH_4 available in the literature to explain the measured radiance. Figure 3 shows a compilation of the VMRs we used. VMR_1 coincides with the profile derived by Drossart et al. (1999) in the 10^{-3} – 10^{-4} hPa region (see Fig. 14a of Moses et al. 2005) and is built below assuming a vertically uniform eddy coefficient, with no (photo)chemical sources or sinks. A similar profile to VMR_1 (VMR_1^R , black dashed curve) was derived in this work (see

Sect. 5) by propagating the uncertainties in the collisional rates of Menard-Bourcin et al. (2005). More generally, the shaded area in grey corresponds to the range of VMRs we derived by considering additional sources of uncertainty, of which the absolute calibration error of the instrument is found to dominate (see Sect. 5.3).

Moses et al. (2005) proposed three different models, of which A and C present the highest and lowest CH_4 abundances, respectively. These profiles provided a reasonable fit to the C_2H_6 and C_2H_2 thermal infrared emissions observed by ISO (Fouchet et al. 2000) and differed by their assumed chemical reaction rates and pathways, and by their assumed eddy mixing coefficient (hence their homopause level). Model A featured an eddy mixing coefficient able to reproduce the CH_4 profile derived from UVS occultation (Yelle et al. 1996) and the methane VMR inferred by Drossart et al. (1999) using the CH_4 fluorescent emissions observed by ISO, while their model C was optimised to reproduce the He airglow (Vervack et al. 1995). For the chemistry, model C explored different reaction rates than model A so as to increase the net production rate of acetylene at high altitudes. In the following, we denote models A and C from Moses et al. (2005) as VMR_2 and VMR_3 , respectively.

The shaded areas in cyan and pink in the figure show the range of VMR profiles derived by Kim et al. (2014, 2020), respectively, from the same ISO measurements. In the former work, the authors found rather low values for the abundance of methane, especially in their lower limit (model D). Even their upper limit, which is similar to the VMR_3 profile from Moses et al. (2005) and is also similar to the best-fitting profile in the updated analysis of Kim et al. (2020), is still significantly lower than the profile derived by Drossart et al. (1999) at pressures lower than 10 mbar, where the bulk emission at $3.3 \mu m$ originates.

When comparing those profiles with previous measurements we find that the larger VMR described by Drossart et al. (1999) agrees very well with the stellar occultation measurements of Yelle et al. (1996). On the contrary, the profile obtained in Kim et al. (2014) and the updated abundance from Kim et al. (2020) fit rather well to the Lyman- α and He 584 Å airglow analysis reported by Moses et al. (2005). The New Horizons ultraviolet stellar occultation measurements reported by Greathouse et al. (2010) also suggest a CH_4 VMR profile similar to model C of Kim et al. (2014). However, the Galileo ASI analysis performed by Seiff et al. (1998) points to a high CH_4 in the 10^{-3} – 10^{-4} mbar region.

Under LTE conditions, the calculated nadir radiance depends directly on the kinetic temperature near the region where the emission emerges, roughly at $\sim 10^{-2}$ – 10^{-4} mbar. In the case of the ISO measurements, however, the measured radiance seems to come from solar pumped excited CH_4 levels in non-LTE (Drossart et al. 1999; Kim et al. 2014, see also below). Drossart et al. (1999) did not discuss the effects of the kinetic temperature profile on the radiance, and Kim et al. (2009, 2014) found that the radiance was almost independent of the kinetic temperature. In contrast, in Sect. 5.1 we show that the effects of T_k on the radiance depend on the collisional rates used in the non-LTE model. Therefore, we considered in our analyses a range of $p-T$ profiles available in the literature (see Fig. 4). Specifically, our nominal profile ($p-T_1$) was computed by Moses et al. (2005); $p-T_2$ was derived using the Galileo probe by Seiff et al. (1998); and $p-T_3$ was obtained by Greathouse et al. (2010) by studying stellar occultation measurements of the New Horizons spacecraft taken during egress. As was discussed in Greathouse et al. (2010), the density profile of the atmosphere was well constrained with the

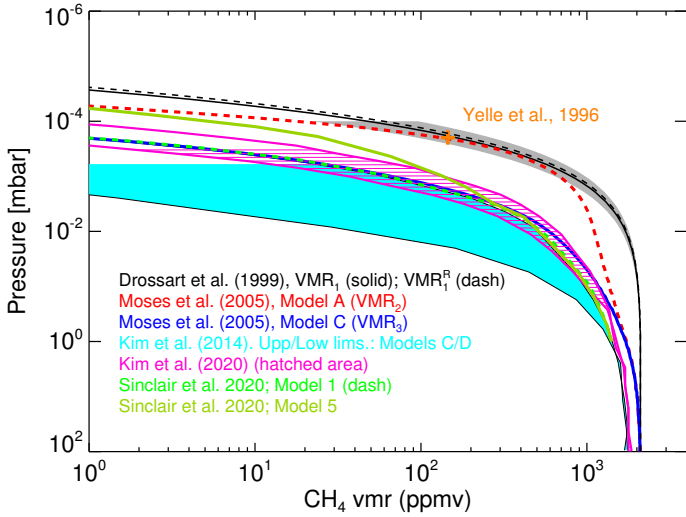


Fig. 3. CH₄ volume mixing ratio profiles considered in this work. The black dashed profile (VMR₁^R) is the CH₄ abundance that we derived in our analyses. The grey shaded area are the errors obtained by propagating the uncertainties of the collisional rates, temperature, and calibration error (see Sect. 5). The rest of the curves correspond to different profiles available in the literature, as labelled in the figure.

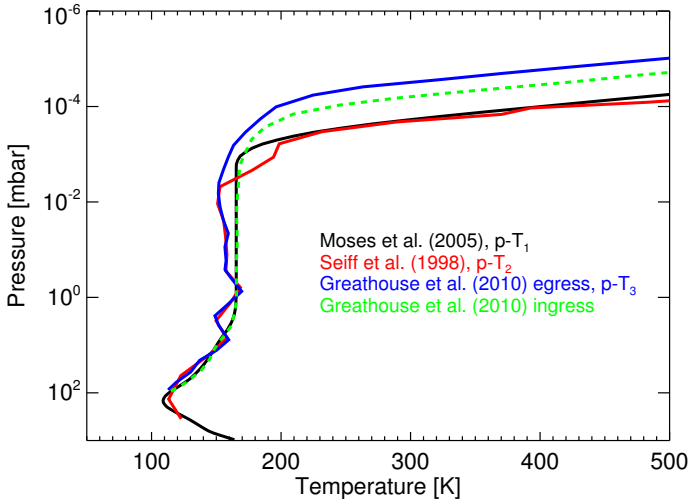


Fig. 4. Pressure–temperature profiles considered in this work. The colours correspond to different profiles available in the literature, as labelled in the figure.

spacecraft, but the inference of the pressure–altitude information was very difficult due to uncertainties in the gravity. Thus, although the shape of the p-T₃ profile is correct, the absolute pressure–altitude reference is more uncertain.

These three profiles encompass rather well the expected range of temperatures near $\sim 10^{-3}$ mbar. However, they are rather different near $\sim 10^{-3}$ mbar, which might have a significant impact on the CH₄ nadir radiances. At lower pressures (higher altitudes), where the emerging nadir radiance is expected to be small, profiles p-T₁ and p-T₂ are very similar with both presenting high temperatures, whereas p-T₃ shows significantly lower values.

4.2. Radiance calculation, contributing bands, and upward contributing radiances

We simulated the nadir radiance calculations by using the Karlsruhe Optimised and Precise Radiative Transfer Algorithm

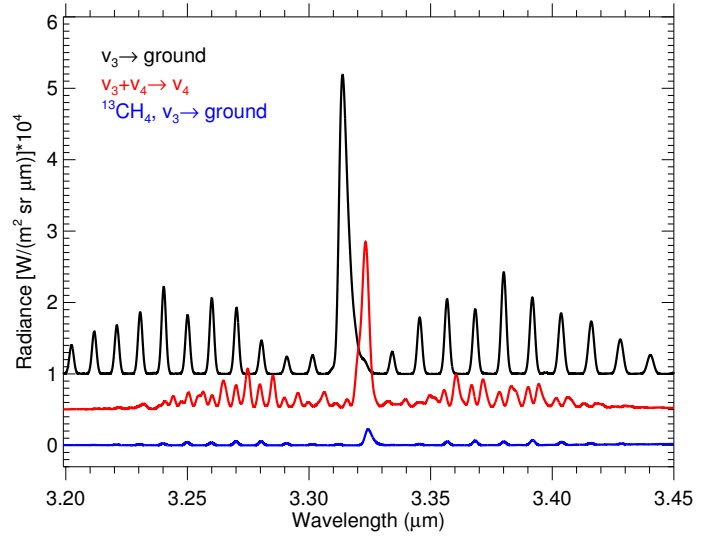


Fig. 5. Contributions of CH₄ bands to the ISO nadir radiances near 3.3 μm for the p-T₁ temperature, the CH₄ VMR₁ profile, and the nominal collisional rates (see Table 1). A vertical offset of 0.5 units was included between the different radiances for clarity.

(KOPRA; Stiller et al. 2002), which is capable of computing radiances under non-LTE conditions. We used the CH₄ linelist presented in Sect. 3 and the line shapes were modelled with a Voigt profile. The radiance was computed internally at a very high spectral resolution (0.0002 cm^{-1}) and later convolved using a Gaussian kernel with a full width at half maximum of 2 cm^{-1} , which corresponds to a resolving power of ~ 1500 at $3.3 \mu\text{m}$. We performed the calculations including the stronger bands near $3.3 \mu\text{m}$ (see Table B.2), which comprises the following bands of the most abundant isotopologue ¹²CH₄: $v_3 \rightarrow \text{ground}$, $v_1 \rightarrow \text{ground}$, $2v_2 \rightarrow \text{ground}$, $v_2 + v_4 \rightarrow \text{ground}$, $v_3 + v_4 \rightarrow v_4$, $v_2 + v_3 \rightarrow v_2$, $2v_3 \rightarrow v_3$, $v_3 + 2v_4 \rightarrow 2v_4$, $v_2 + v_3 + v_4 \rightarrow v_2 + v_4$, and the $v_3 \rightarrow \text{ground}$ band of the second most abundant isotopologue ¹³CH₄. In the figures we also used the HITRAN notation, with the codes ‘61’ and ‘62’ referring to ¹²CH₄ and ¹³CH₄, respectively.

In Fig. 5 we show the radiances of the major contributing bands to the nadir radiance for the p-T₁ and VMR₁ profiles and the nominal non-LTE model (Table 1). We observed that the major contributions come from the fundamental $v_3 \rightarrow \text{ground}$ and the hot $v_3 + v_4 \rightarrow v_4$ bands of the major isotopologue. In addition, the Q branch of the fundamental v_3 band of the ¹³CH₄ isotopologue contributed slightly near $3.325 \mu\text{m}$. The rest of the bands have a negligible contribution to the outgoing radiance. Although the contributions of the different bands strongly depend on the collisional relaxation rates, we observed that the fundamental and hot bands of the ¹²CH₄ isotopologue are always the major contributors for all the sets of collisional rates we tested (see Sect. 5).

We also computed the contribution to the nadir radiance of the different pressure levels for the stronger bands, the $v_3 \rightarrow \text{ground}$ and the hot $v_3 + v_4 \rightarrow v_4$ bands. The atmospheric region from which the radiance emanates depends significantly on the CH₄ concentration, so we computed the contribution functions for the significantly different CH₄ VMR₁ and VMR₃ profiles (see Fig. 3). The resulting contributions are shown in Fig. 6. The radiance of the fundamental band mainly arises at pressure levels from 2×10^{-3} to 5×10^{-5} mbar for the case of the larger VMR₁ profile. For the $v_3 + v_4$ hot band, its emission originates at higher pressures (lower altitudes) from about 2×10^{-3} mbar

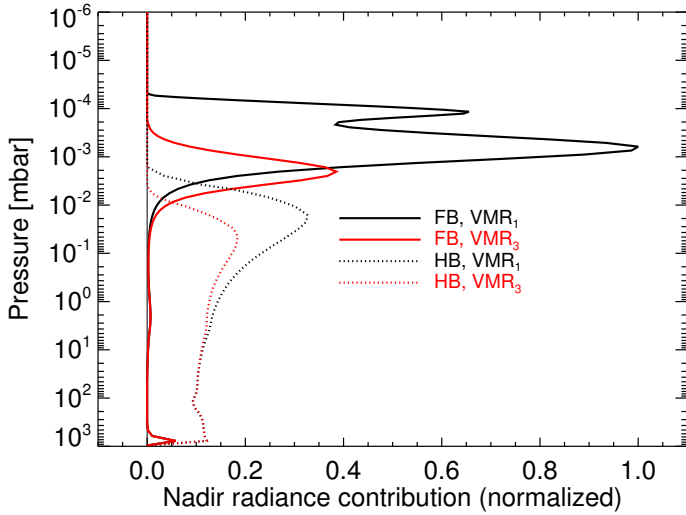


Fig. 6. Contributions to the upward radiance of the fundamental v_3 (FB, solid) and hot v_3+v_4 (HB, dashed) bands of CH_4 at the different pressure levels for the VMR_1 (black) and VMR_3 (red) profiles. The p-T₁ profile and the nominal non-LTE collisional rates of Table 1 were used in all cases. All values have been normalised to the maximum of the v_3 band for VMR_1 .

down to the lowest limit of our model. The significant contribution from high pressures is caused by the rather high excitation temperature (see Fig. 7). As expected, lower CH_4 concentrations (VMR_3) yield lower altitudes of emerging radiance, from 10^{-2} to 2×10^{-4} mbar for the fundamental band and from 10^{-2} to the bottom of the model for the hot band. As the population of the emitting states of these bands increases very rapidly with altitude in these regions (see Fig. 2), the spectral radiance for the VMR_3 profile is then expected to be significantly smaller than for VMR_1 .

5. Results

We modelled the ISO/SWS nadir observations using the non-LTE model described above and the most recent collisional rates measured in the laboratory by Menard-Bourcin et al. (2005) aiming at constraining the CH_4 abundance. As we note in Sect. 4, Drossart et al. (1999) found a rather high CH_4 VMR profile, similar to model A from Moses et al. (2005) (see Fig. 3), but more recent studies by Kim et al. (2014, 2020) derived a significantly smaller CH_4 abundance in the upper stratosphere of Jupiter (see cyan and pink shaded areas in Fig. 3). However, from Fig. 6, we would expect significantly different nadir radiances for the VMR_1 and VMR_3 profiles. Thus, we calculated the vibrational temperatures with the nominal non-LTE collisional rates of Table 1 for both VMR profiles using, in a first instance, p-T₁. The T_{vib} of the emitting energy levels for profile VMR_1 are shown in Fig. 2; and the effects of the different VMR profiles on the population of the major contributing levels are illustrated in Fig. 7. We observed that the vibrational temperatures were higher for the lower VMR_3 profile at pressures in the range of $1-10^{-3}$ mbar. This is explained by the lower CH_4 column density, which allows the solar flux to penetrate deeper into the atmosphere, populating high-energy levels more efficiently than in the case of the VMR_1 profile.

The radiances computed with those VMR profiles are shown in Fig. 8. Here, we observed that using the VMR_3 profile largely underestimated the measured radiance. It is important to note

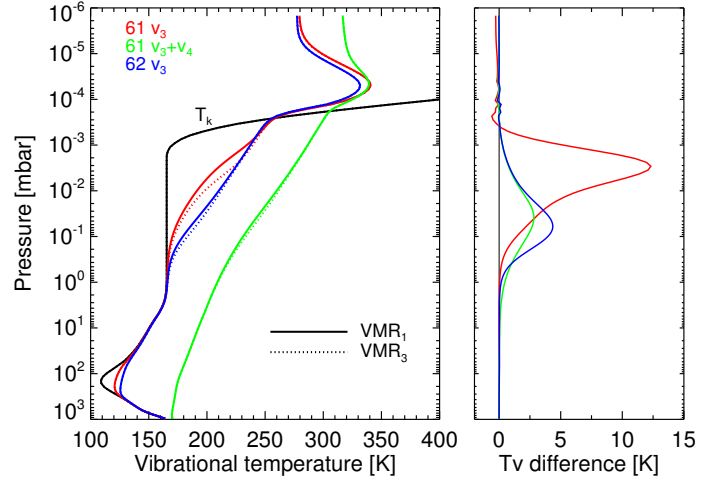


Fig. 7. Effects of the CH_4 VMR on the CH_4 vibrational temperatures for the main energy levels that contribute to the ISO 3.3 μm radiance. The p-T₁ kinetic temperature profile and the nominal collisional rates were used.

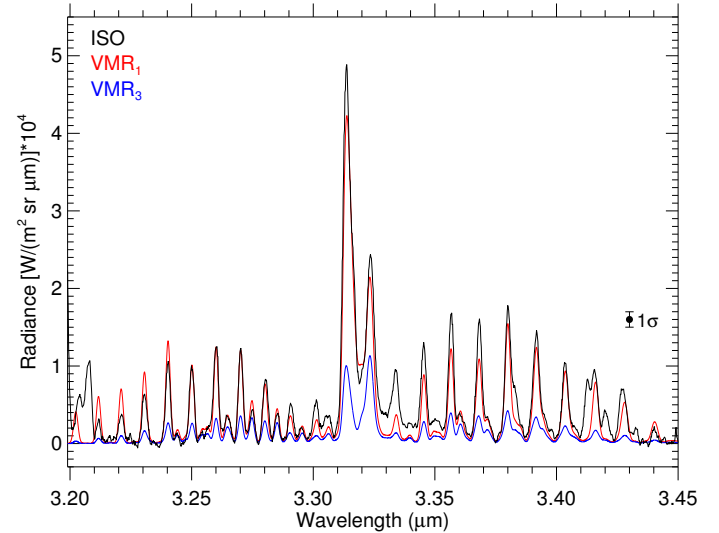


Fig. 8. Measured (black) and synthetic (red, VMR_1 ; blue, VMR_3) spectra. The p-T₁ profile and the nominal collisional rates were used. The 1σ noise error of the measurements is also shown.

that even if the T_{vib} values are higher for VMR_3 , this does not compensate for the fact that the emitting region for this concentration occurs at considerably lower altitudes (see Fig. 6) where the vibrational temperatures are much smaller.

Although the VMR_1 profile allowed us to obtain a reasonable fit, we still underestimated slightly the radiance from the fundamental and the hot bands. Thus, we investigated the effects of the other two variables that mainly control the non-LTE populations of the emitting states and the nadir radiance, specifically the kinetic temperature profile and the collisional relaxation rates. In addition, given the small radiances obtained using VMR_3 , we consider only the highest VMR_1 profile in the following.

5.1. Influence of temperature profiles

We show above that the p-T₁ profile slightly underestimates the measured radiance near the Q branch for the nominal non-LTE model and the VMR_1 profile. Increasing the population of the v_3 level in the $10^{-3}-10^{-4}$ mbar region (see Figs. 2 and 6) requires a

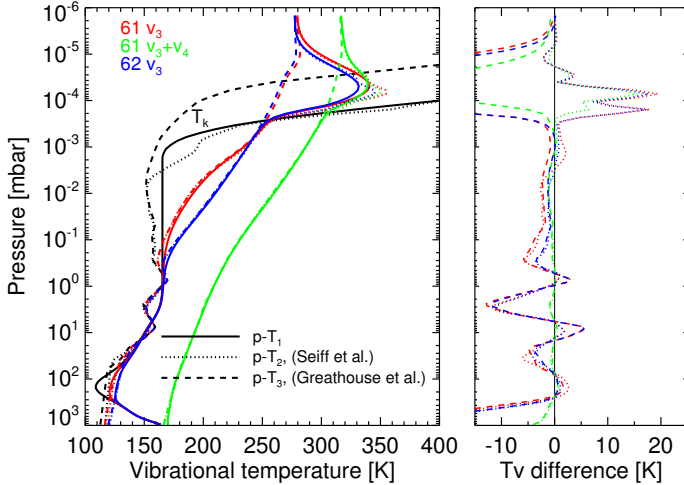


Fig. 9. Effects of the kinetic temperature profiles $p\text{-}T_1$, $p\text{-}T_2$, and $p\text{-}T_3$ on the CH₄ vibrational temperatures for the main energy levels that contribute to the ISO 3.3 μm radiance. The VMR_1 profile and the nominal collisional rates were used.

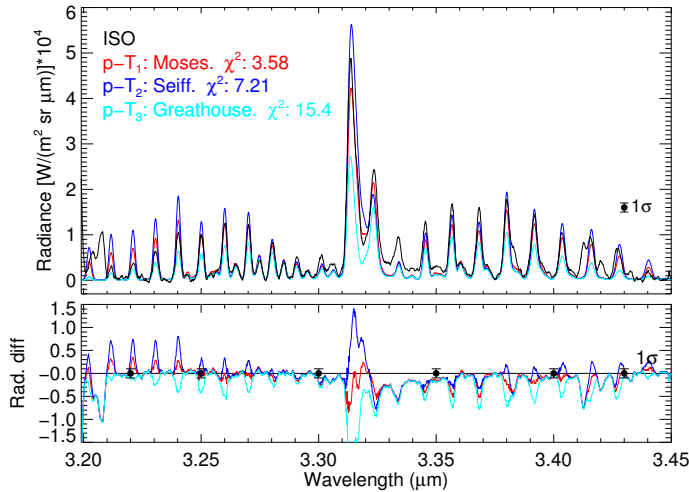


Fig. 10. Measured (black) and synthetic (red, $p\text{-}T_1$; blue, $p\text{-}T_2$; cyan, $p\text{-}T_3$) spectra. The VMR_1 profile and the nominal collisional rates are used. The 1σ noise error of the measurements is also shown. As evidenced by the differences, $p\text{-}T_1$ provides the best fit to the observations.

larger kinetic temperature at those pressure levels. For this purpose, we computed the vibrational temperatures and model nadir radiances using the profile $p\text{-}T_2$ (Seiff et al. 1998) and found a slight overestimation of the measured ISO spectrum in the Q branch of the fundamental band (see Figs. 9 and 10, respectively). This is mainly due to the increase in the T_{vib} of the v_3 level near 10^{-4} mbar (see right panel in Fig. 9). Furthermore, we found a significant overestimation of the radiance in the R branch of the fundamental v_3 band (see lower panel in Fig. 10). This suggests that the temperatures in $p\text{-}T_2$ at these pressure levels might be too large. On the contrary, the v_3+v_4 emission is smaller when using $p\text{-}T_2$, which is caused by the lower kinetic temperature in the contribution region of this band (see Fig. 6). In other words, although the population of v_3+v_4 is in non-LTE at all pressures, it is still affected by thermal relaxation, leading to a vibrational temperature decrease of a few kelvins (see right panel of Fig. 9).

We also performed similar calculations for the colder $p\text{-}T_3$ profile still maintaining the same VMR_1 and the nominal

collisional parameters. The results, as expected, yielded a significantly worse fit than for $p\text{-}T_1$ or $p\text{-}T_2$ due to the much lower vibrational temperatures of the v_3 and v_3+v_4 levels in their contributing layers (i.e. at pressures $\geq 10^{-4}$ mbar and $\geq 10^{-3}$ mbar, respectively).

Interestingly, Kim et al. (2014) found a weak dependence of their radiance calculations with the extreme kinetic temperatures profiles such as the low $p\text{-}T_3$ profile (egress, Greathouse et al. 2010), and the larger temperatures of $p\text{-}T_2$ (Seiff et al. 1998). As we discuss more in depth in Sect. 5.2, this is likely due to their much lower collisional rates. We investigated the temperature dependence of the radiance for the nominal rates (see Fig. 10) and, in contrast with the results obtained by Kim et al. (2014), we observed a significant dependence of the vibrational temperatures on the kinetic temperature. This is a direct consequence of the higher rates of Menard-Bourcin et al. (2005) for the thermalisation of the solar pumped excited states that we used, which lead to a stronger coupling with the kinetic temperature.

5.2. Influence of the collisional rates

The other major source controlling the populations of the emitting levels, and hence the nadir radiance, is the collisional rates that deactivate the solar-pumped energy levels. The rate coefficients used by Drossart et al. (1999) and Kim et al. (2014) differ significantly from those measured in the laboratory by Menard-Bourcin et al. (2005). Kim et al. (2020) used the laboratory values. However, we argue in Sect. 6.1 that the authors misinterpreted the results of Menard-Bourcin et al. (2005) and used an incorrect rate for the collisional relaxation of the CH₄ excited states in collisions with H₂.

Since the rates of Menard-Bourcin et al. (2005) present an uncertainty of $\sim 20\%$, here we have propagated them onto the derived CH₄ profile¹. To do so, we fixed the rates to their minimum (k_{min}) and maximum (k_{max}) values and derived the CH₄ profiles that provided the highest goodness of fit (lowest χ^2) to the observations. Interestingly, we found that for both sets of rates the best fit is obtained when using the VMR_1^R profile in Fig. 3, which is very similar to that derived in Drossart et al. (1999), here denoted VMR_1 . Formally, the best-fitting abundance spans a very narrow area around the dashed curve, not much wider than the line thickness. The reason for this narrow region is explained by the vibrational temperatures obtained for the k_{min} and k_{max} rates (see Fig. 11). For the lower k_{min} rates, the solar pumped v_3 level is decoupled from the kinetic temperature, resulting in an increase of about 2–3 K at $p \geq 2 \times 10^{-4}$ mbar, and a decrease of up 10–15 K in the upper layers; and the opposite occurs for the k_{max} rates. As illustrated in Fig. 6, this band contributes to the nadir radiance mainly in the 10^{-3} – 10^{-4} mbar region, where these increases and/or decreases of its vibrational temperature occur. Thus, for k_{min} the radiance of the region below $\sim 10^{-4}$ mbar increases, while above that pressure it decreases; and the opposite occurs for k_{max} . Therefore, the overall result is that the total radiance hardly changes in the fundamental band (see Fig. 12). Remarkably, the k_{min} case provided a better fit to ISO/SWS data (we note the smaller χ^2 values in Fig. 12), including the three branches of the fundamental band and, particularly, the hot band; the latter is due to the larger population of its upper level for the k_{min} rates below $\sim 2 \times 10^{-4}$ mbar (Fig. 11). This could point to lower collisional rates than those reported by Menard-Bourcin et al. (2005).

¹ In order to be more conservative, we increased the uncertainty intervals to 25%.

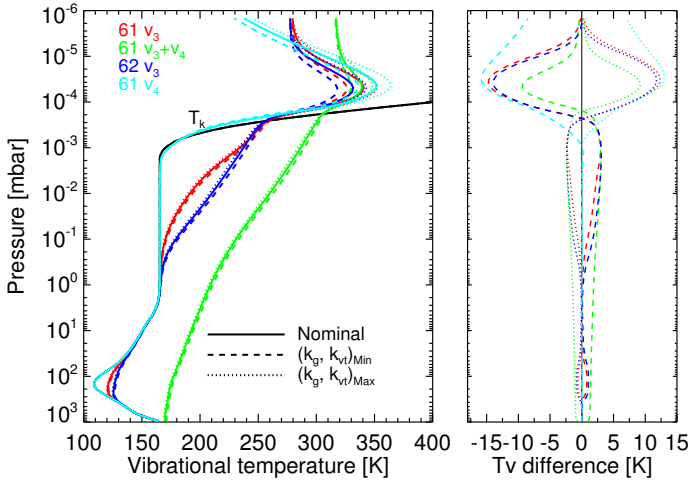


Fig. 11. Effects of perturbing the nominal k_g and k_{v1} rate coefficients by their errors ($\pm 25\%$, factors of 0.75 and 1.25) on the CH_4 vibrational temperatures for the main energy levels that contribute to the ISO 3.3 μm radiance. The VMR_1^R and p-T₁ profiles were used.

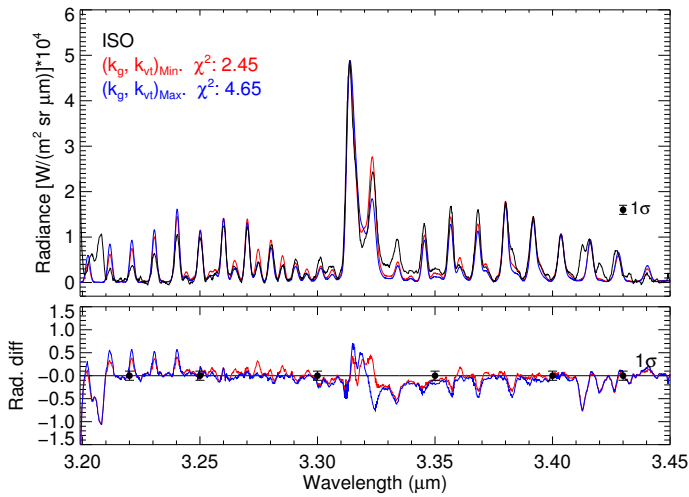


Fig. 12. Effects of perturbing the nominal k_g and k_{v1} rate coefficients on the radiance by their errors. The measured spectrum is shown in black; the p-T₁ and VMR_1^R profiles were used with the k_{min} rates for the model in red, and with k_{max} rates for the blue curve. The 1σ noise error of the measurements is also shown. The relative differences are kept below $\sim 1\%$ in all cases.

5.3. Global error and overall fit

We also estimated the errors in the CH_4 abundances propagated by the calibration uncertainty of 20%. This source of error dominated over the uncertainties of the collisional rates discussed above and of the temperature (estimated to be about 5%). In addition, we considered the errors in the line strengths of the fundamental and hot bands. For the former, the HITRAN 2016 compilation (Gordon et al. 2017) reports an error of 5–10% (uncertainty code = 5). For the hot band there is no reported error in HITRAN, but the comparison of the total strengths in the HITRAN 2016 and McCaSDa databases (Ba et al. 2013) reveals just a 2% difference. Hence, the spectroscopic errors for these measurements are much smaller than the other uncertainties. The total errors of including the uncertainties in these three parameters are shown by the shaded grey area in Fig. 3.

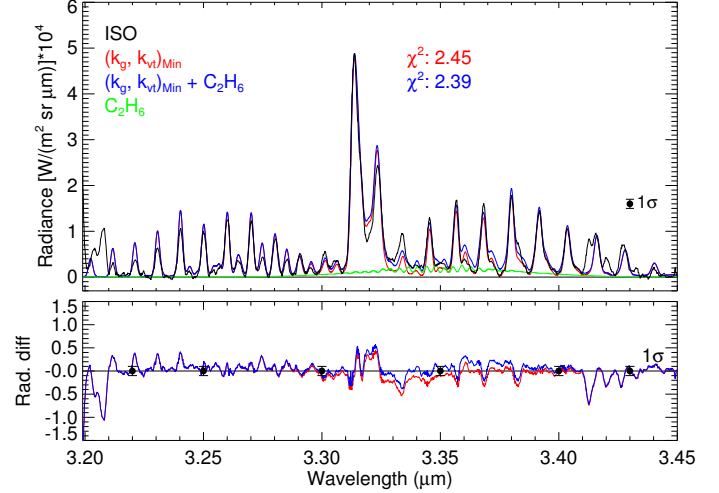


Fig. 13. Measured spectrum (black); model radiance using the p-T₁, the VMR_1^R profile and the lower limit $k_{g,\text{Min}}$ and $k_{v1,\text{Min}}$ rates (red); estimated contribution of C_2H_6 (green); and sum of both contributions (blue). The 1σ noise error of the measurements is also shown. The combined model fits slightly better the measurements (smaller χ^2) as observed in the differences.

The ISO radiances also present H_3^+ features at 3.414 μm , which we did not include in our calculations. Additionally, the emission features at wavelengths shorter than 3.210 μm were not considered in the goodness-of-fit evaluation since they present additional contributions from species other than CH_4 that were not studied here.

Apart from these clear non- CH_4 emissions, there seems to be a systematic underestimation of the ISO radiance from 3.32 to 3.36 μm , which we could not attribute to other CH_4 bands. We note that C_2H_6 has its v_7 band centred at this spectral region. We made a rough estimation of its possible contribution by using the C_2H_6 v_7 linelist of Villanueva et al. (2011), assuming a C_2H_6 abundance profile ten times smaller than the CH_4 VMR_1 profile (Nixon et al. 2007), and adopting the T_{vib} of $\text{CH}_4(v_3)$ for the $\text{C}_2\text{H}_6(v_7)$ state. The results show a better agreement with the ISO radiance (see Fig. 13), suggesting that C_2H_6 may also contribute significantly in this spectral region.

The fit to the ISO radiances still presents an overestimation of the lines of the R branch and an underestimation of the P branch lines. The reason behind these discrepancies is somewhat unclear. In principle, a different temperature profile might solve this issue since the emission from lines of different strengths emanates from different layers that might have different temperatures. However, this would not explain the differences obtained for lines with similar strengths in the two branches. We speculate that a possible explanation could be a drift in the calibration of the baseline of the instrument. In addition, a background continuum emission from the lower atmosphere of Jupiter with a weak wavelength dependency, but modulated by the Planck function, could partially explain the discrepancies. Moreover, the P1 line is also systematically underestimated in all the tests performed. We investigated other CH_4 bands that could contribute in this region. The hot band $v_2+v_3 \rightarrow v_2$ has a dense concentration of lines in the 3.32–3.34 μm range that could enhance the emission of the P1 line. However, we found its contribution to be too weak using the line distribution of HITRAN 2016 and the vibrational temperature computed with our model. It is thus uncertain at the moment which compound could enhance the P1 line emission to the levels observed with ISO.

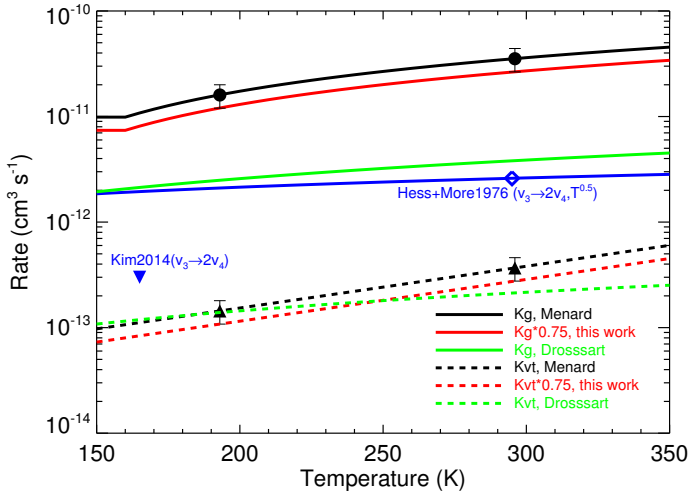


Fig. 14. Collisional rates for the deactivation of the v_3 state, $k_{g,c}$ or $k_{g,d}$ (solid curves), and for the relaxation of the v_4 state, k_{vt} (dashed curves). The rates measured in the laboratory by Menard-Bourcin et al. (2005) are shown with solid circles and triangles, in black, with their respective errors. The rates derived in Drossart et al. (1999) are shown with green curves. The k_{vt} rate measured by Hess & Moore (1976) (blue open diamond) was used in Kim et al. (2014) with a \sqrt{T} -dependence and is indicated by the blue curve. The upper limit of the k_g rate used by Kim et al. (2014) to derive their lower limit model D for the CH₄ abundance is represented with a filled downward triangle in blue. The rates derived in this work are shown in red.

6. Discussion

6.1. Collisional relaxation rates

The reduction of the collisional rates k_g and k_{vt} required to fit the ISO radiance with the VMR₁^R profile is roughly consistent with the lower bound of Menard-Bourcin et al. (2005). The rates derived or used in the previous analyses of Drossart et al. (1999) and Kim et al. (2014) were, however, significantly lower (see Fig. 14), in particular that of the intermode energy transfer process, $k_{g,c}$, which is the major deactivation path for v_3 .

Drossart et al. (1999), who used a simpler CH₄ non-LTE model than ours but a very similar abundance profile, found a rate for the relaxation of the symmetric-asymmetric v_1 and v_3 modes, $a_{vv}(v_3)$, of $95 \text{ s}^{-1} \mu\text{bar}^{-1}$, which corresponds to $2.6 \times 10^{-12} \text{ cm}^3 \text{ s}^{-1}$ at a temperature of 200 K. This rate coefficient is essentially the same measured by Hess & Moore (1976) of $2.6 \times 10^{-12} \text{ cm}^3 \text{ s}^{-1}$ at 295 K. On the contrary, it is about one order of magnitude smaller than that measured by Menard-Bourcin et al. (2005) and also than the value derived in this work (see Fig. 14).

There are several reasons that could explain the different k_g collisional rates derived by Drossart et al. (1999) and in this work. On the one hand, the spectroscopic databases we used are richer and more complete than they were at the time of their publication. In addition, and more importantly, the non-LTE schemes are significantly different, especially in their relaxation pathways.

Hess & Moore (1976) found that the major relaxation path occurred through the $v_3 \rightarrow 2v_4$ process, whereas Menard-Bourcin et al. (2005) (and this work) considered that the intermode energy exchange occurs primarily through $v_3 \rightarrow v_2 + v_4$. Although the energy of the $2v_4$ level is smaller than that of $v_2 + v_4$, this difference is probably not enough to justify the large discrepancy in the relaxation rates. We investigated this possibility by

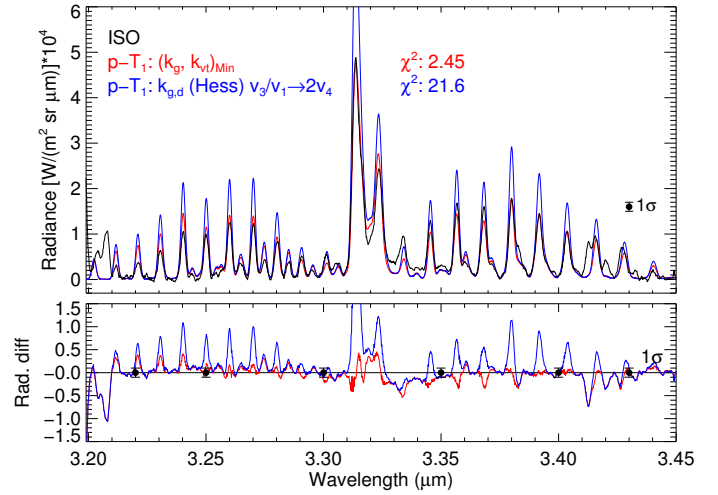


Fig. 15. Measured (black) and synthetic (red and blue) spectra. The red spectrum assumed the p-T₁ and VMR₁^R profiles and the $k_{g,\text{Min}}$ and $k_{v_t,\text{Min}}$ rates. The blue spectrum is obtained assuming the collisional rate $k_{g,d}$ instead of $k_{g,c}$ (see Table 1) and also including the relaxation of v_1 by the same process. The 1σ noise error of the measurements is also shown.

computing the radiances assuming that the $v_3 \rightarrow 2v_4$ path (process $k_{g,d}$ in Table 1) dominates and by including the relaxation of the v_1 mode following the same process. The results showed that the deactivation was still weak in this scenario, leading to large populations of the emitting levels and, consequently, to an overestimation of the radiance (see Fig. 15).

Kim et al. (2014) used the rate of Hess & Moore (1976) to derive their upper limit for the CH₄ VMR. Furthermore, the final values they proposed were significantly lower, which resulted in even lower CH₄ abundances. In particular, their lower limit for the CH₄ VMR was obtained by using a very low relaxation rate for v_3 ('a rough mean of $3.5 \times 10^{-16} \text{ cm}^3 \text{ s}^{-1}$ and $3.0 \times 10^{-13} \text{ cm}^3 \text{ s}^{-1}$ '). The authors estimated this rate to overcome the lack of measurements at low temperatures at that time, and it was based on the relaxations of a different vibrational level, v_2 , and of different partners, for example CH₄(v_2) with H₂, and CD₄(v_2) with H₂ measured at ~ 165 K. According to the measurement of Menard-Bourcin et al. (2005), that value of $\sim 3.0 \times 10^{-13} \text{ cm}^3 \text{ s}^{-1}$ seems to be very small, and hence the low CH₄ abundance derived by Kim et al. (2014) is probably unlikely.

Kim et al. (2020) has more recently reanalysed the ISO measurements using the collisional rates measured by Menard-Bourcin et al. (2005). They report the use of the laboratory rate coefficient k_{v_3} from Menard-Bourcin et al., with values of $2.8 \pm 0.8 \times 10^{-12} \text{ cm}^3 \text{ s}^{-1}$ and $2.45 \pm 0.92 \times 10^{-12} \text{ cm}^3 \text{ s}^{-1}$ at 193 and 296 K, respectively, for the vibrational relaxation of the CH₄ excited states in collisions with H₂. However, k_{v_3} is actually the rate for the vibrational-vibrational exchange of v_3 quanta among CH₄ levels in CH₄-CH₄ collisions (see p. 3117, left column, in Menard-Bourcin et al. 2005) and not the relaxation of the CH₄(v_3, v_b) in collisions with H₂. Instead, we argue that the appropriate rate to use would have been the $k_{v_3 \rightarrow v_2 + v_4}^{\text{H}_2}$ rate in Table 4 of Menard-Bourcin et al. (2005), which is about a factor of ten higher than k_{v_3} .

The effect of using a value for $k_{v_3 \rightarrow v_2 + v_4}^{\text{H}_2}$ (k_g) that is ten times smaller is shown in Fig. A.1 for the VMR₁ profile. As expected, we obtained a large overestimation of the radiances. We also attempted to reproduce the Kim et al. (2020) results by using this low rate and the methane abundances that they derived (VMR₃

in Fig. 3). The results are shown in Fig. A.2. In this case we observed that the ISO radiances in the fundamental band are quite well reproduced, but the contribution of the hot band is largely overestimated. We note that the residuals very closely resemble the contribution of the hot band itself (see the red curve in Fig. 5). Therefore, their lower $k_{v_3 \rightarrow v_2+v_4}^{H_2}$ rate is very likely the reason behind the significantly lower CH₄ VMRs they obtained for the homopause, when compared to our results.

As for the vibrational-thermal (V–T) energy transfer (k_{vt}), which controls the thermalisation of the v_4 and v_2 bending quanta, we note that the values derived by Drossart et al. (1999) and those obtained here are very similar to those measured in the laboratory by Menard-Bourcin et al. (2005) and certainly within the measured 20% uncertainties (dashed lines in Fig. 14). Perhaps the temperature dependence of the rate coefficient at high temperatures in Drossart et al. (1999) is slightly weak.

6.2. CH₄ abundance

We show that the best fit to ISO/SWS measurements is obtained using the CH₄ abundance from the VMR₁^R profile. This profile is very similar to the one used in Drossart et al. (1999) from 10^{−3} to 10^{−4} mbar, and is also similar to other profiles reported in the literature, for example to the profiles retrieved from the stellar occultation measurements by Yelle et al. (1996), and to those obtained in the Galileo ASI analysis performed by Seiff et al. (1998). On the contrary, it is significantly larger than the upper limit for the CH₄ VMR profile obtained by Kim et al. (2014) and the updated abundance reported in Kim et al. (2020), both resulting from the analysis of the same ISO/SWS spectra. As we discuss in previous sections, a possible explanation for the discrepancy with the former is the use of very different collisional rates. As for the latter work, we argued in Sect. 6.1 that the authors might have misinterpreted the results of Menard-Bourcin et al. (2005) and used an incorrect rate for the relaxation of CH₄ levels in collisions with H₂, which lead them to a lower methane abundance than in this work.

Very recently, Sinclair et al. (2020) used ground-based IRTF-TEXES high-resolution spectra to compare the homopause location in auroral and non-auroral regions and inferred the CH₄ abundance near the homopause. They did not use the 3.3 μm methane emission in the near-infrared, but studied mid-infrared CH₄ radiances arising from the v_4 level, and the CH₃ emission near 600 cm^{−1}. Figure 3 shows the range of the CH₄ VMR that these authors obtained. They found that at latitudes outside the auroral regions, their models 1 (low VMR) and 5 (medium VMR) yielded the best fits to their observed spectra at latitudes of 50°N and 68°N, respectively. The differences between the two models are relatively small, however. Their model 1 is very similar to the CH₄ VMR₃ profile of Moses et al. (2005), and model 5 shows a higher abundance above ~10^{−3} mbar, approaching the VMR₁ profile at lower pressures. Our best-fit CH₄ abundances in the VMR₁^R profile are significantly higher than those of Sinclair et al. (2020) near the homopause, at pressures in the range of 10^{−2}–10^{−4} mbar. A possible explanation for this discrepancy could be that the mid-infrared emission measurements they analysed might be probing slightly higher atmospheric heights than ISO/SWS data (see their Fig. 4). In addition, they considered the CH₄(v_4) emission to be in LTE, whereas our model shows that the population of this band starts departing from LTE (with lower populations) at about 5×10^{-4} mbar (see Fig. 11). Using the smallest non-LTE populations that we obtained for this level would result in higher retrieved CH₄ abundances, which would be in better agreement with the VMR₁^R profile.

Accurately assessing the impact of our derived vertical profile of methane on the atmospheric energy budget, haze distribution, or kinetic temperature profile is challenging, as it would require a self-consistent modelling of the atmospheric radiative and chemical processes. However, our results do suggest that methane is carried to higher layers than in some of previous works (see Fig. 3). This translates into a stronger atmospheric mixing in the upper stratosphere and lower thermosphere. In addition, as the photolysis of methane and molecular diffusion deplete the high atmosphere of hydrocarbons coolants, the larger methane abundance hints at a slightly higher homopause and thermospheric base.

7. Conclusions

We have analysed ISO/SWS nadir measurements of CH₄ emission at 3.3 μm arising from the homopause region in the atmosphere of Jupiter. By using a comprehensive non-LTE model to compute the population of the energy levels and the collisional relaxation rates (considering their uncertainties) reported by Menard-Bourcin et al. (2005), we have presented the obtained abundance profile of CH₄, the kinetic and vibrational temperature structures, and the collisional relaxation parameters that allow us to best fit the observed infrared radiance.

Our analyses strongly favour a rather high volume mixing ratio of CH₄ at μ-bar pressures. This is in good agreement with the results obtained by Drossart et al. (1999), who analysed the same observations; with Yelle et al. (1996), who studied stellar occultation using the Voyager Ultraviolet Spectrometer; and with Seiff et al. (1998), who performed the Galileo ASI analysis. On the contrary, our results do not agree with the low CH₄ abundance provided by Kim et al. (2014) from the ISO/SWS data, although the latter results are in line with those derived by Moses et al. (2005) from helium airglow spectra and the New Horizons ultraviolet stellar occultation measurements reported by Greathouse et al. (2010). The very different collisional rate coefficients used in Kim et al. (2014), lower than those of Menard-Bourcin et al. (2005), are likely behind this discrepancy. Further, our derived methane abundance near the μ-bar pressure level is significantly higher than the value reported in Kim et al. (2020). However, an incorrect application of the collisional rates of Menard-Bourcin et al. (2005) in the latter work might be behind their lower CH₄ concentration.

We have propagated the uncertainties in the absolute calibration of ISO/SWS, in the collisional rates of Menard-Bourcin et al. (2005), in the p-T profiles, and in the line strengths of the fundamental and hot bands onto the derived methane abundance. We find that the calibration uncertainties dominate over any other source of error. The final range of methane abundances we find still supports higher methane abundances than previously reported in the upper atmosphere of Jupiter. Interestingly, the minimum values of the collisional relaxation rates (i.e. a conservative reduction of 25%) allowed us to best fit the observed radiance. In addition, we have found that the effects of the temperature profile on the radiance are dependent on the collisional rate coefficients. For the low rates used in Drossart et al. (1999) and Kim et al. (2014), this dependence is negligible due to the strong decoupling. However, when using the rate coefficients of Menard-Bourcin et al. (2005), the effect becomes significant.

Acknowledgements. We thank the anonymous referee for their insightful reading of the manuscript and very useful suggestions. A.S.L. and I.S. acknowledge funding from the European Research Council (ERC) under the European Union's Horizon 2020 research and innovation program under grant agreement No

694513. IAA-CSIC authors acknowledge financial support from the Agencia Estatal de Investigación of the Ministerio de Ciencia, Innovación y Universidades through projects Ref. PID2019-110689RB-I00/AEI/10.13039/501100011033 and the Centre of Excellence “Severo Ochoa” award to the Instituto de Astrofísica de Andalucía (SEV-2017-0709).

References

- Appleby, J. F. 1990, *Icarus*, **85**, 355
- Ba, Y. A., Wenger, C., Surleau, R., et al. 2013, *J. Quant. Spectr. Rad. Transf.*, **130**, 62
- de Graauw, T. 1996, *A&A*, **315**, L49
- Drossart, P., Fouchet, T., Crovisier, J., et al. 1999, in *The Universe as Seen by ISO*, eds. P. Cox, & M. F. Kessler (Paris: ESA SP), 427
- Encrenaz, T., Drossart, P., Feuchtgruber, H., et al. 1999, *Planet. Space Sci.*, **47**, 1225
- Fouchet, T., Lellouch, E., Bézard, B., et al. 2000, [arXiv:astro-ph/0002273]
- Funke, B., López-Puertas, M., García-Comas, M., et al. 2012, *J. Quant. Spectr. Rad. Transf.*, **113**, 1771
- García-Comas, M., López-Puertas, M., Funke, B., et al. 2011, *Icarus*, **214**, 571
- Gordon, I. E., Rothman, L. S., Hill, C., et al. 2017, *J. Quant. Spectr. Rad. Transf.*, **203**, 3
- Greathouse, T. K., Gladstone, G. R., Moses, J. I., et al. 2010, *Icarus*, **208**, 293
- Hess, P., & Moore, C. B. 1976, *J. Chem. Phys.*, **65**, 2339
- Hess, P., Kung, A., & Moore, C. 1980, *J. Chem. Phys.*, **72**, 5525
- Jurado-Navarro, A. A., López-Puertas, M., Funke, B., et al. 2015, *J. Geophys. Res.*, **120**, 8002
- Kessler, M. F., Steinz, J. A., Anderegg, M. E., et al. 1996, *A&A*, **500**, 493
- Kim, S. J., Geballe, T. R., Seo, H. J., & Kim, J. H. 2009, *Icarus*, **202**, 354
- Kim, S. J., Sim, C. K., Sohn, M. R., & Moses, J. I. 2014, *Icarus*, **237**, 42
- Kim, S. J., Sim, C. K., Geballe, T. R., et al. 2020, *Icarus*, **348**, 113852
- López-Puertas, M., & Taylor, F. W. 2001, *Non-LTE Radiative Transfer in the Atmosphere* (Singapore: World Scientific Publication)
- Menard-Bourcin, F., Boursier, C., Doyennette, L., & Menard, J. 2005, *J. Phys. Chem. A*, **109**, 3111
- Miller, S., Stallard, T., Tennyson, J., & Melin, H. 2013, *J. Phys. Chem. A*, **117**, 9770
- Moses, J. I., Fouchet, T., Bézard, B., et al. 2005, *J. Geophys. Res.*, **110**, E08001
- Nixon, C. A., Achterberg, R. K., Conrath, B. J., et al. 2007, *Icarus*, **188**, 47
- Panka, P., Fouchet, T., Kutepov, A., et al. 2018, *AAS/Div. Planet. Sci. Meeting Abs.*, **50**, 214
- Rothman, L. S., Gordon, I. E., Babikov, Y., et al. 2013, *J. Quant. Spectr. Rad. Transf.*, **130**, 4
- Seiff, A., Kirk, D. B., Knight, T. C. D., et al. 1998, *J. Geophys. Res. Planets*, **103**, 22857
- Sinclair, J. A., Greathouse, T. K., Giles, R. S., et al. 2020, *Planet. Sci. J.*, **1**, 85
- Stiller, G. P., von Clarmann, T., Funke, B., et al. 2002, *J. Quant. Spectr. Rad. Transf.*, **72**, 249
- Vervack, J. R. J., Sandel, B. R., Gladstone, G. R., McConnell, J. C., & Parkinson, C. D. 1995, *Icarus*, **114**, 163
- Villanueva, G. L., Mumma, M. J., & Magee-Sauer, K. 2011, *J. Geophys. Res.*, **116**, E08012
- Yelle, R. V., Young, L. A., Vervack, R. J., et al. 1996, *J. Geophys. Res. Planets*, **101**, 2149

Appendix A: ISO radiances using k_g rates 10 times smaller

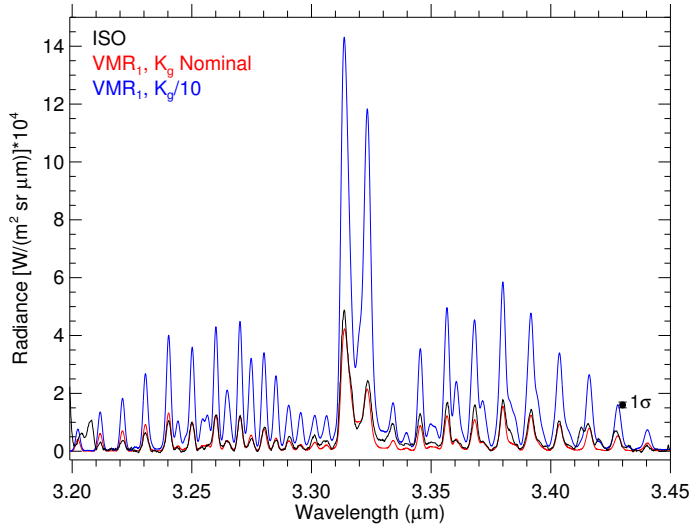


Fig. A.1. Effects of using a k_g rate ten times lower than in Table 1. Shown are the measured (black) and synthetic (red and blue) spectra. The red spectrum assumes the p-T₁ and VMR₁ profiles and the k_g rate in Table 1. The blue spectrum was obtained assuming a collisional rate k_g that is times smaller. The 1σ noise error of the measurements is also shown.

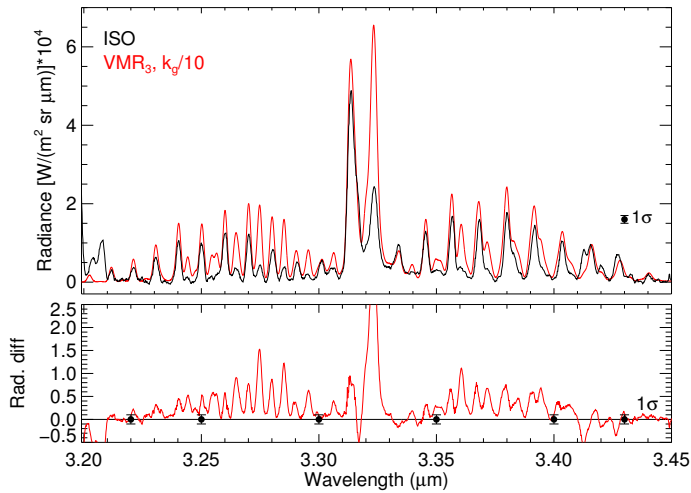


Fig. A.2. Simulations using a k_g rate ten times smaller than in Table 1 and the CH₄ VMR₃ profile. The ISO measured (black) spectrum is also shown for reference. The residuals very closely resemble the hot band contribution (see red curve in Fig. 5). The 1σ noise error of the measurements is also shown.

Appendix B: CH₄ energy levels and vibrational bands

Vibrational energy levels and bands considered in the non-LTE model.

Table B.1. CH₄ vibrational energy levels included in the model (updated from García-Comas et al. 2011).

Group	ID ^(a)	Level	Energy (cm ⁻¹)
	1	Ground	0.00
V _{7.6}	2	v_4	1310.76
	3	v_2	1533.33
V _{3.3}	4	$2v_4$	2608.69
	6	v_2+v_4	2838.26
	7	v_1	2916.48
	8	v_3	3019.50
	9	$2v_2$	3064.48
V _{2.3}	29	$3v_4$	3870.50
	44	v_2+2v_4	4123.00
	10	v_1+v_4	4223.46
	11	v_3+v_4	4321.67
	12	v_2+v_3	4540.65
V _{1.7}	56	$4v_4$	5161.10
	30	v_3+2v_4	5588.00
	102	$v_1+v_2+v_4$	5775.00
	103	$v_2+v_3+v_4$	5861.00
	13	$2v_3$	6024.28
	1	Ground (62)	0.00
V _{7.6,iso=2}	2	v_4 (62)	1292.00
V _{3.3,iso=2}	4	$2v_4$ (62)	2588.16
	8	v_3 (62)	2999.06

Notes. ^(a) HITRAN ID.

Table B.2. CH₄ vibrational bands included in the model.

Iso	Upper level	Lower level	(IDu)	(IDl)	$\bar{\nu}_0$ (cm ⁻¹)	A [†] (s ⁻¹)	Notes [‡]
1	2v ₂	v ₃	9	8	44.98	2.374e-06 ^a	–
1	v ₁	v ₂ +v ₄	7	6	78.22	1.890e-05	–
1	v ₃	v ₁	8	7	103.02	2.464e-05 ^a	–
1	2v ₂	v ₁	9	7	148.00	6.095e-07 ^a	–
1	v ₃	v ₂ +v ₄	8	6	181.24	2.686e-04 ^b	–
1	v ₂	v ₄	3	2	222.57	5.539e-05	–
1	2v ₂	v ₂ +v ₄	9	6	226.22	9.291e-05	–
1	v ₂ +v ₄	2v ₄	6	4	229.57	6.766e-05	–
1	v ₁	2v ₄	7	4	307.79	2.164e-04	–
1	v ₃	2v ₄	8	4	410.81	8.929e-05	–
1	2v ₂	2v ₄	9	4	455.79	2.006e-05	–
1	4v ₄	v ₂ +v ₃	56	12	620.45	1.408e-05 ^a	–
1	3v ₄	2v ₂	29	9	806.02	1.382e-05 ^a	–
1	4v ₄	v ₃ +v ₄	56	11	839.43	3.527e-04 ^a	–
1	3v ₄	v ₃	29	8	851.00	6.644e-05 ^a	–
1	4v ₄	v ₁ +v ₄	56	10	937.64	1.016e-03 ^a	–
1	3v ₄	v ₁	29	7	954.02	1.437e-04 ^a	–
1	3v ₄	v ₂ +v ₄	29	6	1032.24	4.249e-03 ^a	–
1	4v ₄	v ₂ +2v ₄	56	44	1038.10	2.393e-02 ^a	–
1	v ₃ +2v ₄	v ₂ +v ₃	30	12	1047.35	4.783e-03 ^a	–
1	v ₂ +2v ₄	2v ₂	44	9	1058.52	1.550e-03 ^a	–
1	2v ₄	v ₂	4	3	1075.36	1.114e-03 ^a	–
1	v ₂ +2v ₄	v ₃	44	8	1103.50	1.491e-03 ^a	–
1	v ₁ +v ₄	2v ₂	10	9	1158.98	3.361e-03 ^a	–
1	v ₁ +v ₄	v ₃	10	8	1203.96	5.998e-02 ^a	–
1	v ₂ +2v ₄	v ₁	44	7	1206.52	8.738e-03 ^a	–
1	v ₁ +v ₂ +v ₄	v ₂ +v ₃	102	12	1234.35	1.077e-01 ^a	–
1	v ₃ +v ₄	2v ₂	11	9	1257.19	8.968e-02 ^a	–
1	3v ₄	2v ₄	29	4	1261.81	6.621e+00 ^a	–
1	v ₃ +2v ₄	v ₃ +v ₄	30	11	1266.33	3.826e+00 ^a	–
1	v ₂ +2v ₄	v ₂ +v ₄	44	6	1284.74	4.675e+00 ^a	–
1	4v ₄	3v ₄	56	29	1290.60	9.904e+00 ^a	–
1	2v ₄	v ₄	4	2	1297.93	4.817e+00	RT
1	v ₃ +v ₄	v ₃	11	8	1302.17	2.236e+00 ^a	–
1	v ₂ +v ₄	v ₂	6	3	1304.93	2.267e+00	–
1	v ₁ +v ₄	v ₁	10	7	1306.98	2.229e+00 ^a	–
1	v ₄	Ground	2	1	1310.76	2.325e+00	RT
1	v ₂ +v ₃ +v ₄	v ₂ +v ₃	103	12	1320.35	2.391e+00 ^a	–
1	v ₃ +2v ₄	v ₁ +v ₄	30	10	1364.54	1.522e-01 ^a	–
1	v ₁	v ₂	7	3	1383.15	1.007e-01	RT
1	v ₁ +v ₄	v ₂ +v ₄	10	6	1385.20	4.126e-01 ^a	–
1	v ₃ +v ₄	v ₁	11	7	1405.19	3.006e-02 ^a	–
1	v ₁ +v ₂ +v ₄	v ₃ +v ₄	102	11	1453.33	1.746e-01 ^a	–
1	v ₃ +2v ₄	v ₂ +2v ₄	30	44	1465.00	3.261e-01 ^a	–
1	v ₂ +v ₃	2v ₂	12	9	1476.17	4.877e-01 ^a	–
1	v ₃ +v ₄	v ₂ +v ₄	11	6	1483.41	3.318e-01 ^a	–
1	2v ₃	v ₂ +v ₃	13	12	1483.63	6.624e-01 ^a	–
1	v ₃	v ₂	8	3	1486.17	3.213e-01	–
1	v ₂ +2v ₄	2v ₄	44	4	1514.31	9.028e-02 ^a	–
1	v ₂ +v ₃	v ₃	12	8	1521.15	4.681e-02 ^a	–
1	v ₂ +v ₄	v ₄	6	2	1527.50	5.846e-02	–
1	2v ₂	v ₂	9	3	1531.15	1.034e-01	RT
1	v ₂	Ground	3	1	1533.33	4.569e-02	RT
1	v ₂ +v ₃ +v ₄	v ₃ +v ₄	103	11	1539.33	1.400e-01 ^a	–
1	v ₁ +v ₂ +v ₄	v ₁ +v ₄	102	10	1551.54	1.071e-01 ^a	–
1	v ₁	v ₄	7	2	1605.72	3.004e-02	–
1	v ₁ +v ₄	2v ₄	10	4	1614.77	1.029e-01 ^a	–
1	v ₂ +v ₃	v ₁	12	7	1624.17	2.907e-02 ^a	–
1	v ₂ +v ₃ +v ₄	v ₁ +v ₄	103	10	1637.54	9.270e-02 ^a	–
1	v ₁ +v ₂ +v ₄	v ₂ +2v ₄	102	44	1652.00	1.247e-01 ^a	–

Table B.2. continued.

Iso	Upper level	Lower level	(IDu)	(IDl)	$\bar{\nu}_0$ (cm ⁻¹)	A [†] (s ⁻¹)	Notes [‡]
1	v_2+v_3	v_2+v_4	12	6	1702.39	8.252e-01 ^a	–
1	$2v_3$	v_3+v_4	13	11	1702.61	1.335e+00 ^a	–
1	v_3	v_4	8	2	1708.74	8.407e-01	–
1	v_3+v_4	$2v_4$	11	4	1712.98	1.151e+00 ^a	–
1	v_3+2v_4	$3v_4$	30	29	1717.50	1.176e+00 ^a	–
1	$v_2+v_3+v_4$	v_2+2v_4	103	44	1738.00	1.096e+00 ^a	–
1	$2v_2$	v_4	9	2	1753.72	4.775e-02	–
1	$2v_3$	v_1+v_4	13	10	1800.82	5.262e-02 ^a	–
1	$2v_3$	v_2+2v_4	13	44	1901.28	1.915e-01 ^a	–
1	$v_1+v_2+v_4$	$3v_4$	102	29	1904.50	4.939e-02 ^a	–
1	v_2+v_3	$2v_4$	12	4	1931.96	6.019e-03 ^a	–
1	$v_2+v_3+v_4$	$3v_4$	103	29	1990.50	1.708e-02 ^a	–
1	$4v_4$	v_3	56	8	2141.60	2.600e-03 ^a	–
1	$2v_3$	$3v_4$	13	29	2153.78	1.193e-01 ^a	–
1	$4v_4$	v_1	56	7	2244.62	2.863e-05 ^a	–
1	$4v_4$	v_2+v_4	56	6	2322.84	2.593e-03 ^a	–
1	$3v_4$	v_2	29	3	2337.17	7.914e-04 ^a	–
1	v_3+2v_4	$2v_2$	30	9	2523.52	1.024e-02 ^a	–
1	$4v_4$	$2v_4$	56	4	2552.41	3.281e-01 ^a	–
1	$3v_4$	v_4	29	2	2559.74	1.502e-01	–
1	v_3+2v_4	v_3	30	8	2568.50	1.112e-01 ^a	–
1	v_2+2v_4	v_2	44	3	2589.67	5.780e-02 ^a	–
1	$2v_4$	Ground	4	1	2608.69	5.438e-02	RT, Sun
1	v_3+2v_4	v_1	30	7	2671.52	6.977e-03 ^a	–
1	v_1+v_4	v_2	10	3	2690.13	4.369e-03	–
1	$v_1+v_2+v_4$	$2v_2$	102	9	2710.52	2.226e-01 ^a	–
1	v_3+2v_4	v_2+v_4	30	6	2749.74	2.137e-01 ^a	–
1	$v_1+v_2+v_4$	v_3	102	8	2755.50	2.959e-01 ^a	–
1	v_3+v_4	v_2	11	3	2788.34	2.706e-02	–
1	$v_2+v_3+v_4$	$2v_2$	103	9	2796.52	9.335e-02 ^a	–
1	v_2+2v_4	v_4	44	2	2812.24	5.756e-01	–
1	v_2+v_4	Ground	6	1	2838.26	3.897e-01	RT, Sun
1	$v_2+v_3+v_4$	v_3	103	8	2841.50	8.059e-01 ^a	–
1	$v_1+v_2+v_4$	v_1	102	7	2858.52	4.928e-01 ^a	–
1	v_1+v_4	v_4	10	2	2912.70	5.254e-01	–
1	v_1	Ground	7	1	2916.48	5.539e-03	RT
1	$v_1+v_2+v_4$	v_2+v_4	102	6	2936.74	1.321e+00 ^a	–
1	$v_2+v_3+v_4$	v_1	103	7	2944.52	1.059e+00 ^a	–
1	$2v_3$	$2v_2$	13	9	2959.80	4.295e-01 ^a	–
1	v_3+2v_4	$2v_4$	30	4	2979.31	1.945e+01 ^a	Sun
1	$2v_3$	v_3	13	8	3004.78	4.554e+01 ^a	Sun
1	v_2+v_3	v_2	12	3	3007.32	2.251e+01	RT
1	v_3+v_4	v_4	11	2	3010.91	2.374e+01	RT
1	v_3	Ground	8	1	3019.50	2.493e+01	RT, Sun
1	$v_2+v_3+v_4$	v_2+v_4	103	6	3022.74	2.383e+01 ^a	–
1	$2v_2$	Ground	9	1	3064.48	7.446e-02	RT
1	$2v_3$	v_1	13	7	3107.80	6.919e-01 ^a	–
1	$v_1+v_2+v_4$	$2v_4$	102	4	3166.31	9.926e-01 ^a	–
1	$2v_3$	v_2+v_4	13	6	3186.02	3.714e+00 ^a	–
1	v_2+v_3	v_4	12	2	3229.89	9.060e-02	–
1	$v_2+v_3+v_4$	$2v_4$	103	4	3252.31	2.348e-01 ^a	–
1	$2v_3$	$2v_4$	13	4	3415.59	1.262e+00 ^a	–
1	$4v_4$	v_2	56	3	3627.77	3.688e-04 ^a	–
1	$4v_4$	v_4	56	2	3850.34	1.477e-01 ^a	–
1	$3v_4$	Ground	29	1	3870.50	3.617e-02	RT, Sun
1	v_3+2v_4	v_2	30	3	4054.67	1.448e-02 ^a	–
1	v_2+2v_4	Ground	44	1	4123.00	2.829e-02	–
1	v_1+v_4	Ground	10	1	4223.46	1.567e+00	RT, Sun
1	$v_1+v_2+v_4$	v_2	102	3	4241.67	1.254e+00 ^a	–
1	v_3+2v_4	v_4	30	2	4277.24	1.224e+00 ^a	–
1	v_3+v_4	Ground	11	1	4321.67	5.222e-01	RT, Sun

Table B.2. continued.

Iso	Upper level	Lower level	(IDu)	(IDl)	$\bar{\nu}_0$ (cm ⁻¹)	A [†] (s ⁻¹)	Notes [‡]
1	$\nu_2+\nu_3+\nu_4$	ν_2	103	3	4327.67	7.700e-01 ^a	–
1	$\nu_1+\nu_2+\nu_4$	ν_4	102	2	4464.24	1.298e-01 ^a	–
1	$2\nu_3$	ν_2	13	3	4490.95	2.979e-01 ^a	–
1	$\nu_2+\nu_3$	Ground	12	1	4540.65	2.121e-01	RT, Sun
1	$\nu_2+\nu_3+\nu_4$	ν_4	103	2	4550.24	2.013e-01 ^a	–
1	$2\nu_3$	ν_4	13	2	4713.52	1.094e-02	–
1	$4\nu_4$	Ground	56	1	5161.10	1.007e-03	–
1	$\nu_3+2\nu_4$	Ground	30	1	5588.00	2.854e-02 ^a	Sun
1	$\nu_1+\nu_2+\nu_4$	Ground	102	1	5775.00	3.419e-03 ^a	–
1	$\nu_2+\nu_3+\nu_4$	Ground	103	1	5861.00	5.474e-02 ^a	Sun
1	$2\nu_3$	Ground	13	1	6024.28	3.289e-01 ^b	Sun
2	ν_4	Ground	2	1	1292.00	2.055e+00	RT
2	$2\nu_4$	ν_4	4	2	1296.16	4.632e+00	RT
2	$2\nu_4$	Ground	4	1	2588.16	5.133e-02	RT, Sun
2	ν_3	Ground	8	1	2999.06	2.298e+01	RT, Sun

Notes. [†] Einstein coefficient at 250 K calculated from the HITRAN 2016 edition (Gordon et al. 2017). ^a Calculated from the MeCaSDa database (Ba et al. 2013). ^b Calculated from the HITRAN 2012 database (Rothman et al. 2013). [‡] RT: Full radiative transfer among atmospheric layers is included. Sun: The absorption of solar radiation in this band is important.